

Sizing of 3-D Arbitrary Defects Using Magnetic Flux Leakage Measurements

Maryam Ravan¹, Reza Khalaj Amineh¹, Slawomir Koziel², Natalia K. Nikolova¹, and James P. Reilly¹

¹Department of Electrical and Computer Engineering, McMaster University, Hamilton, ON L8S 4K1, Canada

²School of Science and Engineering, Reykjavik University, IS-103 Iceland

In this paper, we propose a new procedure to estimate the shape of the opening and the depth profile of an arbitrary three-dimensional (3-D) defect from magnetic flux leakage (MFL) measurements. We first use the Canny edge detection algorithm to estimate the shape of the defect opening. Then we use an inversion procedure based on the space mapping (SM) methodology in order to approximate the defect depth profile efficiently. To demonstrate the accuracy of the proposed inversion technique, we reconstruct defects of arbitrary shapes from simulated MFL signals. The procedure is then tested with experimental data of two metal-loss defects. In both cases, the proposed approach shows good agreement between the actual and estimated defect parameters.

Index Terms—Arbitrary defect, edge detection, magnetic flux leakage (MFL), sizing, space mapping optimization.

I. INTRODUCTION

MAGNETIC FLUX LEAKAGE (MFL) is one of the most widely used electromagnetic nondestructive testing (NDT) techniques and has been used for oil and gas pipeline inspection since the 1960s [1]–[12] in order to find metal-loss regions usually caused by corrosion, fatigue, etc. Like in other NDT techniques, solution of the inverse problem for predicting the shape and size of defects from measured MFL probe output signals is of utmost interest in the community.

The solutions of inverse problem could be classified either as non-model based or model based. Non-model based approaches attempt to solve the inverse problem by using signal processing techniques by establishing a relationship between the signal and the geometry of the defect. Typical examples of such methods use neural networks to build such functional relationships ([1]–[3]). These models are fast but are limited to the specific region of defect geometries for which the neural network is trained.

Model based methods, on the other hand, usually employ a physical model as a forward model that simulates the measured signal to solve the inverse problem. In these methods, the forward problem is solved repetitively in all iterative optimization loops, using an initial guess for the unknown defect parameters. Three major groups of forward models involve numerical models such as the finite-element method (FEM) (e.g., [4]–[6]), analytical models (e.g., [7]–[10]), and neural networks (e.g., [11]–[13]). Numerical models provide accurate results but they are computationally expensive while analytical models and neural networks are fast but less accurate due to the approximations made in deriving them.

To take the advantage of the accuracy of the FEM and the speed of the analytical approach, one can use the space mapping (SM) optimization method [14]–[19] to characterize the defect parameters. SM exploits the accurate but time consuming “fine” model (i.e., FEM forward model) and the fast and less accurate “coarse” model (i.e., analytical formulas) in an iterative manner. Provided that the misalignment between the fine model and the coarse model is not severe, SM-based algorithms typically provide satisfactory results after only a few evaluations of the fine model. This method has recently been used as an efficient tool in crack parameter estimation from FEM simulated MFL signals [20]. However, in practice, defects have arbitrary opening shape and arbitrary depth profiles.

Dealing with arbitrary defects under practical conditions, i.e., without any *a priori* knowledge, requires the optimization of a large number of parameters which has an adverse impact on the efficiency, robustness, and convergence rate of the optimization process. Usually, some predetermined simple geometries are used for arbitrary defects in order to decrease the number of parameters. Examples include rectangular, cylindrical [20], and integer stair-case block defects [21]. These procedures cannot be applied to real defects with complicated shapes.

Here, to reduce the number of optimization parameters while keeping the defect arbitrary, we propose a procedure with the following two separate consecutive steps.

- Estimate the shape of the defect opening (top view) by applying an edge detection algorithm directly to the MFL measured signal.
- Approximate the defect depth profile parameters using an SM optimization method.

To validate the efficiency of the proposed inversion method, simulated and real arbitrary defects are reconstructed.

The next section describes the estimation of the shape of the defect opening. Then the FEM and analytical models for prediction of the MFL response are explained in Sections III and IV, respectively. Section V briefly describes the SM algorithm. The method for defect geometry estimation is then proposed in Section VI. Finally, the efficiency of the proposed inversion is validated by the results of several case studies in Section VII.

Manuscript received October 25, 2008; revised June 12, 2009; accepted November 04, 2009. First published December 11, 2009; current version published March 19, 2010. Corresponding author: M. Ravan (e-mail: mravan@ece.mcmaster.ca).

Color versions of one or more of the figures in this paper are available online at <http://ieeexplore.ieee.org>.

Digital Object Identifier 10.1109/TMAG.2009.2037008

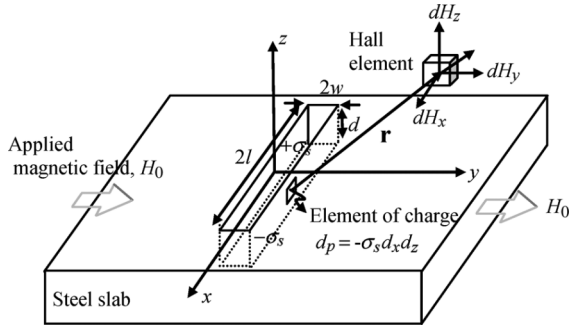


Fig. 1. Dipolar representation of a rectangular defect.

II. ESTIMATION OF THE SHAPE OF THE DEFECT OPENING

The basic principle of the MFL measurement is that a powerful magnet is used to magnetize the ferromagnetic metal. At areas where there is a defect, a high fraction of magnetic field leaks from the wall of the defect into the air. This flux leakage is measured by a Hall sensor and used to estimate the dimensions of the defect. Fig. 1 shows the schematic diagram of the MFL method for detection of a defect with rectangular geometry.

The position of the peaks in the spatial gradient of the two-dimensional (2-D) measured magnetic field can give us a proper approximation of the shape of the defect opening when we apply an appropriate edge detection. Here we chose the Canny edge detection algorithm, which is very successful in achieving the optimum edges [22]. The Canny edge detector first smooths the image to eliminate noise. It then finds the image gradient to highlight regions with high spatial derivatives. The algorithm then tracks along these regions and suppresses any pixel that is not at the maximum (non-maximum suppression). The gradient array is then further reduced by hysteresis. Hysteresis is used to track along the remaining pixels that have not been suppressed. The hysteresis uses two thresholds, (T_1, T_2) , and if the magnitude is below the lower threshold T_1 , it is set to zero (made a non-edge). If the magnitude is above the higher threshold T_2 , it is made an edge and if the magnitude is between the two thresholds, then it is set to zero unless there is a path from this pixel to a pixel with a gradient above T_2 .

III. FEM SIMULATIONS TO PREDICT MFL RESPONSE

The electromagnetic phenomena underlying MFL systems comply with Maxwell's equations in a nonlinear permanent magnet. This leads to [23]

$$\nabla \times \nabla \times \mathbf{A} = \mu_0(\mathbf{J} + \nabla \times \mathbf{M}) \quad (1)$$

where μ_0 , \mathbf{J} , and \mathbf{A} are the permeability of vacuum, the current density, and the magnetic vector potential, respectively. The magnetization \mathbf{M} is a nonlinear function of $\mathbf{B} = \nabla \times \mathbf{A}$. Therefore, the nonlinear (1) is solved iteratively.¹

A nonlinear FEM using Maxwell v. 11 [24] is used for simulating the 3-D magnetic field around and inside a surface defect

¹Throughout, we denote 3-D field vectors in bold, while matrices and column vectors are in bold italics.

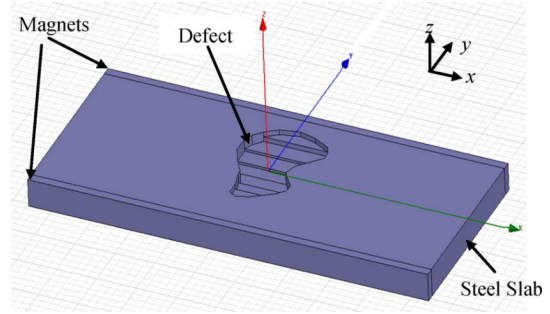
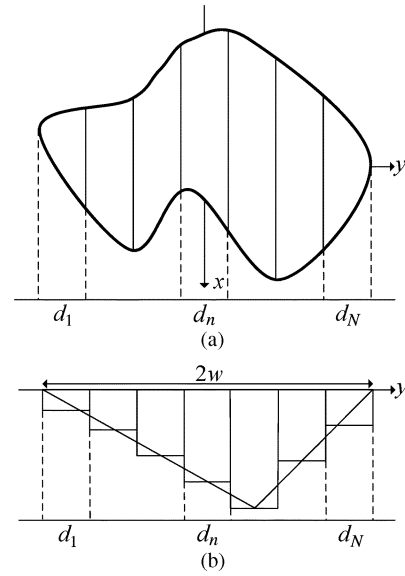


Fig. 2. 3-D view of the simulated model in Maxwell v. 11.

Fig. 3. Representation of: (a) defect opening, and (b) depth profile with N equidistant defects of constant depth.

in a steel slab [20]. Fig. 2 shows the model geometry where the steel slab is magnetized in the y -direction with two parallel magnets. This simplified model of the magnetizers can reduce the computational time while maintaining good accuracy [20], [25].

To simplify the simulation, the defect depth profile is approximated in a stair-case manner as shown in Fig. 2. The flat stair-case elements have the same constant width along y while their lengths along x are determined by the defect opening. Their depths d_n ($n = 1, 2, \dots, N$) approximate the variation of the defect bottom along y as shown in Fig. 3.

IV. ANALYTICAL APPROACH TO PREDICT MFL RESPONSES

In analytical approaches, the magnetic leakage flux is formulated mathematically by a dipole model [7]–[10]. In this model, the magnetic field is distributed homogeneously in the part of the metal which is not disturbed by the defect and the repulsion of the magnetic flux lines from the defect is represented by considering the defect being filled homogeneously by magnetic dipoles with magnetic moments oriented in the same direction, which is opposite to the direction of the applied magnetic field (y direction). These magnetic dipoles generate a magnetic

field outside the metal, which is equivalent to a leakage magnetic field. The magnetic field $d\mathbf{H}$ generated at a distance \mathbf{r} by each element of charge, $dp = \sigma_s dx dz$, is given by [10]

$$d\mathbf{H}(x, y, z) = \frac{dp}{4\pi r^3} \cdot \mathbf{r}. \quad (2)$$

The magnetic field \mathbf{H} is calculated at each observation point by integrating the magnetic field due to all charge elements dp . Therefore, for a defect with a simple rectangular shape of length $2l$, width $2w$, and depth d with constant polarity σ_s extending from $-l$ to $+l$ in the x direction, from $-w$ to w in the y direction and from 0 to $-d$ in the z direction (see Fig. 1), the distribution of the y -component of the leakage magnetic field at a point with coordinates x, y, z is obtained by [10]

$$H_{yr}(x, y, z) = \sigma_s / 4\pi \left(\int_{-d}^0 \int_{-l}^l \frac{(y+w) dx' dz'}{((x-x')^2 + (y+w)^2 + (z-z')^2)^{3/2}} - \int_{-d}^0 \int_{-l}^l \frac{(y-w) dx' dz'}{((x-x')^2 + (y-w)^2 + (z-z')^2)^{3/2}} \right) \quad (3)$$

where the first term represents the magnetic field that leaks from the wall with poles of constant positive polarity ($y = -w$) and the second term represents the magnetic field that leaks from the wall with poles of equal negative polarity ($y = +w$). The solution of the integrations yields the following simple expression:

$$H_{yr}(x, y, z) = \sigma_s / 4\pi \times \left(\tan^{-1} \left(\frac{(z+d)(x+l)}{(y+w)\sqrt{(x+l)^2 + (y+w)^2 + (z+d)^2}} \right) - \tan^{-1} \left(\frac{z(x+l)}{(y+w)\sqrt{(x+l)^2 + (y+w)^2 + z^2}} \right) - \tan^{-1} \left(\frac{(z+d)(x-l)}{(y+w)\sqrt{(x-l)^2 + (y+w)^2 + (z+d)^2}} \right) + \tan^{-1} \left(\frac{z(x-l)}{(y+w)\sqrt{(x-l)^2 + (y+w)^2 + z^2}} \right) - \tan^{-1} \left(\frac{(z+d)(x+l)}{(y-w)\sqrt{(x+l)^2 + (y-w)^2 + (z+d)^2}} \right) + \tan^{-1} \left(\frac{z(x+l)}{(y-w)\sqrt{(x+l)^2 + (y-w)^2 + z^2}} \right) + \tan^{-1} \left(\frac{(z+d)(x-l)}{(y-w)\sqrt{(x-l)^2 + (y-w)^2 + (z+d)^2}} \right) - \tan^{-1} \left(\frac{z(x-l)}{(y-w)\sqrt{(x-l)^2 + (y-w)^2 + z^2}} \right) \right). \quad (4)$$

For an arbitrary defect of width $2w$ (Fig. 3), each sub-defect can be approximated by a set of M tightly packed rectangular defects of width $w_r = 2w/(MN)$ such that the i th rectangular defect of the n th sub-defect has a length of $l_{n,i}$ and a depth

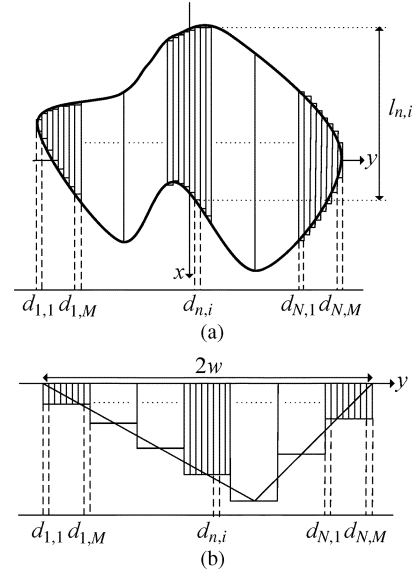


Fig. 4. Representation of each sub-defect of the investigated defect by M rectangular defects with width $2w/(MN)$, length $l_{n,i}$, and depth $d_{n,i}$.

of $d_{n,i}$ ($i = 1, 2, \dots, M$) which is equal to the depth of the n th sub-defect (Fig. 4). The larger the value of M the more accurate analytical responses are obtained. The intensity of the leakage field in a given point above the metal is approximated by a sum of the leakage fields of the corresponding set of rectangular defects:

$$H_y(x, y, z) = \sum_{n=1}^N \sum_{i=1}^M H_{yr,n,i}(x, y, z). \quad (5)$$

In this model, it is assumed that each rectangular defect is filled homogeneously by magnetic dipoles, i.e., the surface density of the magnetic charge has a constant value on both walls of the rectangular defect. This simplifying assumption leads to errors in calculating the leakage field, which indicates that the distribution of the magnetic dipoles σ_s along the defect depth is not constant [8]. Here, since we use the analytical model as a fast and less accurate “coarse” model, we can afford the simplifying assumption.

V. SPACE MAPPING OPTIMIZATION

Consider an actual model $\mathbf{R}_f(x_f) : R^n \rightarrow R^m$ as a “fine” model. The set of variables \mathbf{x}_f that minimize $U(\mathbf{R}_f(\mathbf{x}_f)) = \|\mathbf{R}_f(\mathbf{x}_f) - \mathbf{R}_{\text{spec}}\|$ is

$$\mathbf{x}_f^* = \arg \min_{\mathbf{x}_f} U(\mathbf{R}_f(\mathbf{x}_f)) \quad (6)$$

where $\mathbf{R}_{\text{spec}} = [R_{\text{spec},1} \dots R_{\text{spec},m}]^T$ is the set of target responses. If solving (6) is computationally too expensive, a cheap model $\mathbf{R}_c(\mathbf{x}_c) : R^n \rightarrow R^m$ is introduced as the coarse model. This coarse model is faster to evaluate but is less accurate.

The problem

$$\mathbf{x}_c^* = \arg \min_{\mathbf{x}_c} U(\mathbf{R}_c(\mathbf{x}_c)) \quad (7)$$

where $U(\mathbf{R}_c(\mathbf{x}_c)) = \|\mathbf{R}_c(\mathbf{x}_c) - \mathbf{R}_{\text{spec}}\|$, is easy to solve, but \mathbf{x}_c^* is likely to differ from \mathbf{x}_f^* . To compensate the mismatch between

the two models, a mapping function $p : R^n \rightarrow R^n$, relating the fine and coarse model variables, is defined as

$$\mathbf{x}_c = p(\mathbf{x}_f) \quad (8)$$

such that the surrogate model $\mathbf{R}_s(\mathbf{x}_c)$ satisfies

$$\mathbf{R}_s(\mathbf{x}_c) = \mathbf{R}_c(p(\mathbf{x}_f)) \approx \mathbf{R}_f(\mathbf{x}_f) \quad (9)$$

in a region of interest. Mapping p is obtained in a so-called parameter extraction process (cf. [19]) where the misalignment between the surrogate and the fine model is minimized.

Having p , the direct optimization of the fine model can be avoided and instead a solution

$$\hat{\mathbf{x}}_f = p^{-1}(\mathbf{x}_c^*) \quad (10)$$

is considered as a good estimate of \mathbf{x}_f^* , where \mathbf{x}_c^* is the optimal coarse model solution (7) [20]. The SM technique aims at finding the mapping p , which is iteratively updated until the satisfactory fine model solution is found.

VI. DEFECT GEOMETRY ESTIMATION

The inverse problem is solved as follows. A color map of the 2-D measured signal is provided and is considered to be an image of the defect opening. The Canny edge detection algorithm is then applied to this image to extract the edge of the defect opening. The Canny algorithm first smoothes an image by convolving with a Gaussian mask to eliminate most of the noise. Next, the algorithm attempts to detect edges at the maxima of the gradient modulus taken in the direction of the gradient. This algorithm produces an edge strength and direction at each pixel in the smoothed image [22]. We apply the Canny edge detector in Matlab [26] to the color map images.

The shape of the defect opening is then used to simulate the coarse and fine models within the SM optimization algorithm, which estimates the defect depth profile parameters. FEM simulations serve as the fine model and the analytical formulas given by (3) and (5) (implemented in Matlab [26]) serve as the coarse model. We use the SMF system [27] to perform the SM optimization.

The termination condition for the SM algorithm has the following form:

$$\Delta x = \frac{\|\mathbf{x}^{(i+1)} - \mathbf{x}^{(i)}\|}{\|\mathbf{x}^{(i)}\|} < \delta \quad (11)$$

where $\|\cdot\|$ is the l_2 -norm, $\mathbf{x}^{(i)}$, $i = 0, 1, \dots$ is the sequence of solutions produced by the SM algorithm, and δ is a user defined constant such that $0 < \delta \ll 1$.

VII. RESULTS

Here we examine the accuracy of the proposed method with simulated and experimental MFL data. First, we simulate three defects with complex geometries, shown in Fig. 5(a)–(c). The thickness of the slab is 5.6 mm. The target MFL responses are the y -component distributions of the magnetic field calculated at the surface of the metal using FEM simulations. Figs. 6(a), 7(a),

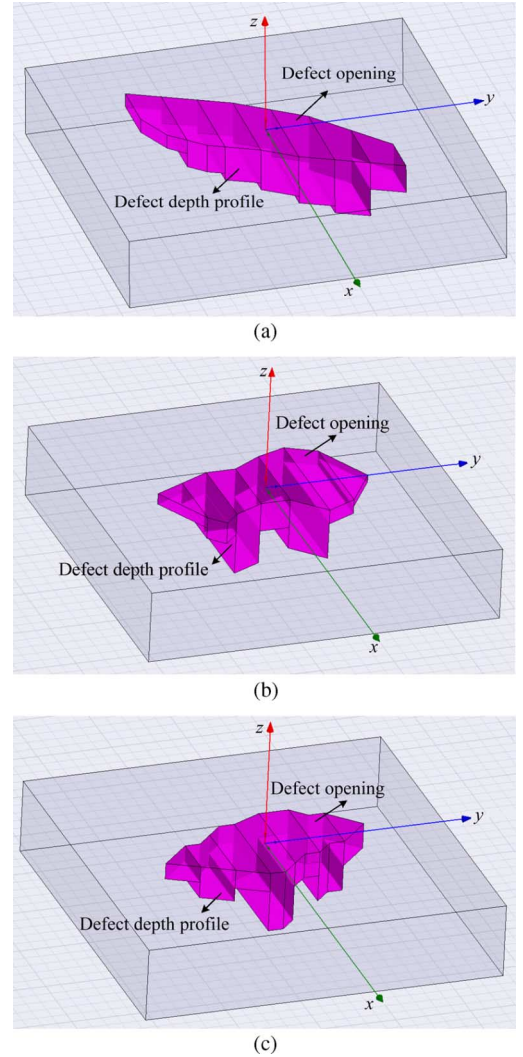


Fig. 5. 3-D view of three different arbitrary defects.

and 8(a) show the 2-D color map of the surface MFL signal for three defects. We can estimate the edge of the defect opening (top view) accurately by applying the Canny edge detector to these color maps. Figs. 6(b), 7(b), and 8(b) show the reconstructed edges of the respective defects, which follow the actual edges in Fig. 5 accurately. We can use these edges to model the defect opening in the coarse and fine models.

To approximate the depth profile, we consider $N = 7$ sub-defects in the fine model and divide each sub-defect into $M = 2w/(N \times w_r)$ rectangular defects with width $w_r = 2$ mm in the coarse model. We impose the constraints $d_1 = d_2/2$ and $d_7 = d_6/2$ in Fig. 5. Therefore, the inversion is a five-variable optimization problem for the depths $\{d_2, d_3, \dots, d_6\}$. One can increase the level of discretization N , to improve the accuracy of the defect geometry estimation at the expense of increasing the time and complexity.

It should be noted that the performance of the SM algorithm depends on the similarity between the fine model and the coarse model, which can be expressed in rigorous mathematical terms (e.g., [19]). Here, because the maximum amplitudes of the MFL distributions obtained from the coarse and the fine models are

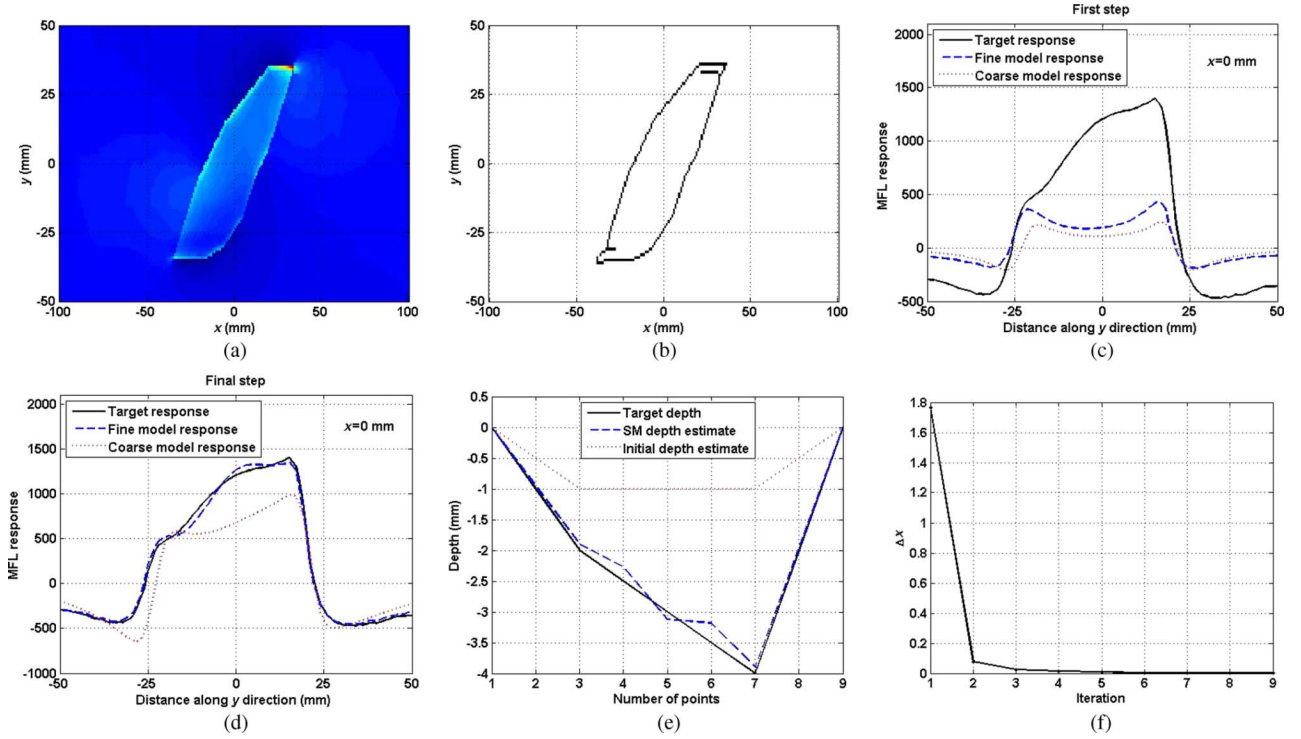


Fig. 6. (a) 2-D color map of the MFL signal for the defect of Fig. 5(a); (b) the defect opening (top view) detected by the Canny algorithm; (c), (d) comparison of the target MFL response with the MFL responses of the coarse and fine models obtained at initial and optimal points respectively, at $x = 0$ mm and (e) their corresponding defect depth profile; (f) Δx in (11) versus iterations.

substantially different, we use a scaling surface to align them. We assume that the length and depth of each rectangular defect of the coarse model lie between two limiting cases, that is

$$5 \text{ mm} \leq l \leq 80 \text{ mm} \quad (12a)$$

$$0.1 \text{ mm} \leq d \leq 4.5 \text{ mm}. \quad (12b)$$

The surface describes the coefficient which multiplies the coarse model response of each rectangular defect to match the maximum of the corresponding fine model response within the search region. We construct this surface using the coarse and fine model responses for a set of twelve sample points defining six quadrant sub-surfaces that cover the whole 2-D parameter space of rectangular defects [Fig. 9(a)]. Each sub-surface is defined by four points. Table I shows the cracks that are used to define the six sub-surfaces in Fig. 9(a). We use the following 2-D inter/extrapolation formula to evaluate the sub-surface M at any \mathbf{s} :

$$M(s_1, s_2) = A \cdot s_1 + B \cdot s_2 + C \cdot s_1 \cdot s_2 + D \quad (13)$$

where A , B , C , and D are constants which are computed using the corresponding four points of the sub-surface. For rectangular defects, the following points are used to construct the scaling surface: $\mathbf{s}^1 = [1 \ 1]^T$, $\mathbf{s}^2 = [1 \ 25]^T$, $\mathbf{s}^3 = [1 \ 50]^T$, $\mathbf{s}^4 = [1 \ 75]^T$, $\mathbf{s}^5 = [2.5 \ 1]^T$, ..., $\mathbf{s}^9 = [4 \ 1]^T$, ..., $\mathbf{s}^{12} = [4 \ 75]^T$. Fig. 9(b) shows the scaling surface based on the mentioned points. Once we have the scaling surface $M(\mathbf{s})$, we use the scaling factor at each \mathbf{s} to adjust the level of the coarse model response to that of the fine model. The total leakage field of the defect in a given point above the metal is then approximated by a sum of the scaled leakage fields of the rectangular defects:

$$H_y(x, y, z) = \sum_{n=1}^N \sum_{i=1}^M \gamma_{n,i} H_{y_{r_{n,i}}}(x, y, z). \quad (14)$$

where $\gamma_{n,i}$ is the scaling factor for the i th rectangular defect of the n th sub-defect.

SM optimization is performed using the input space mapping surrogate model of the form $\mathbf{R}_s(\mathbf{x}) = \mathbf{R}_c(p(\mathbf{x})) = \mathbf{R}_c(\mathbf{x} + \mathbf{c})$ where \mathbf{x} is the defect depth profile vector and the mapping vector \mathbf{c} is obtained through the parameter extraction process. This particular model has been chosen because it provides sufficient match with the fine model. We use the termination condition (11) with δ equal to 0.001.

Figs. 6(c), 7(c), and 8(c) and Figs. 6(d), 7(d), and 8(d) compare the target MFL response with the MFL responses of the coarse and fine models obtained at initial and optimal points for the three investigated defects, respectively. We use a row of the 2-D surface MFL signal that passes along the crack ($H_y(0, y, 0)$) as a target signal for the SM optimization. Comparisons of the actual depth profile with the initial and optimal estimated depth profiles are shown in Figs. 6(e), 7(e), and 8(e). To illustrate the performance of SM algorithm, Figs. 6(f), 7(f), and 8(f) show the convergence characteristic of SM algorithm based on (11). As the figures show, the SM algorithm converges in few iterations. A quantitative comparison of these results can also be found in Table II where the mean relative error (MRE) between the original defect depth profile, x_i ($i = 1, 2, \dots, 5$) and its reconstructed counterpart, \hat{x}_i ($i = 1, 2, \dots, 5$), is defined as

$$\text{MRE}(\hat{x}) = \frac{1}{7} \sum_{i=1}^7 \frac{|x_i - \hat{x}_i|}{x_i} \times 100. \quad (15)$$

As can be seen in Table II, the SM optimization converges to the solution after few fine model evaluations and the value of MRE in the three cases is less than 10%. In order to confirm the speed and accuracy of the SM optimization algorithm, Table II

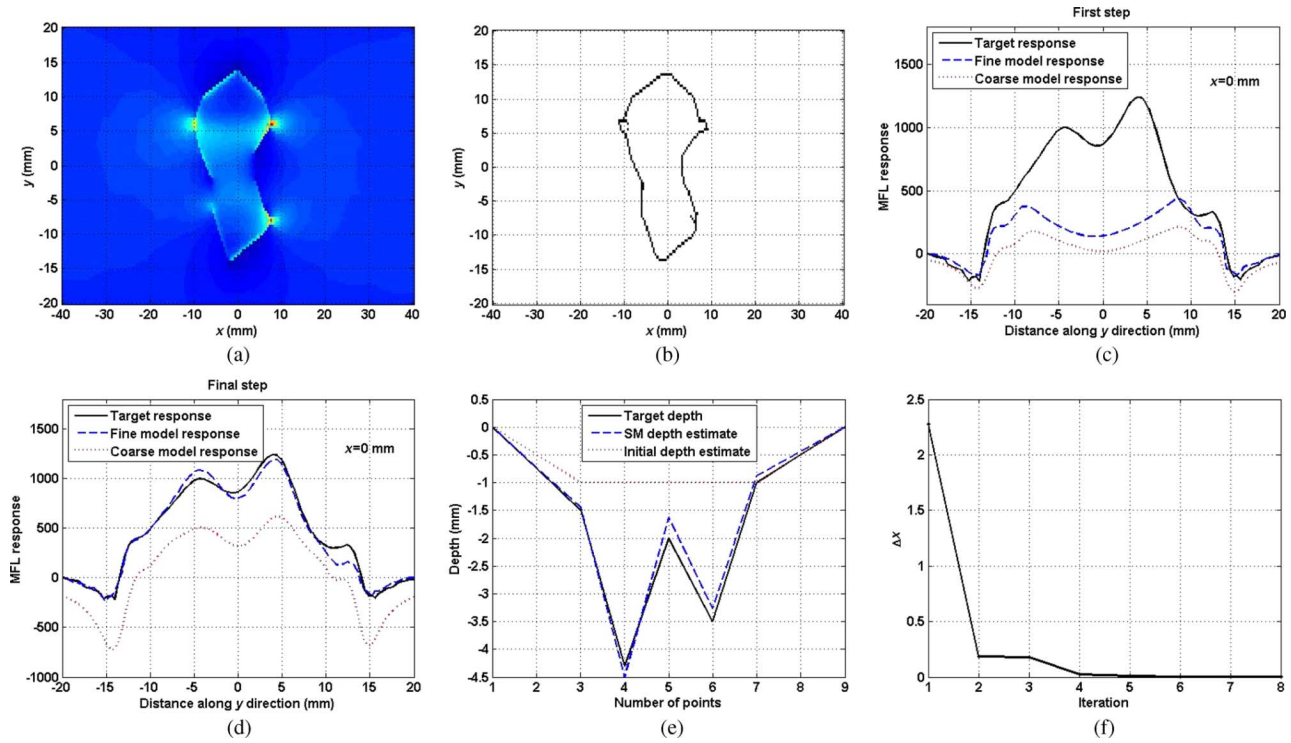


Fig. 7. (a) 2-D color map of the MFL signal for the defect of Fig. 5(b); (b) the defect opening (top view) detected by the Canny algorithm; (c), (d) comparison of the target MFL response with the MFL responses of the coarse and fine models obtained at initial and optimal points respectively, at $x = 0$ mm and (e) their corresponding defect depth profile; (f) Δx in (11) versus iterations.

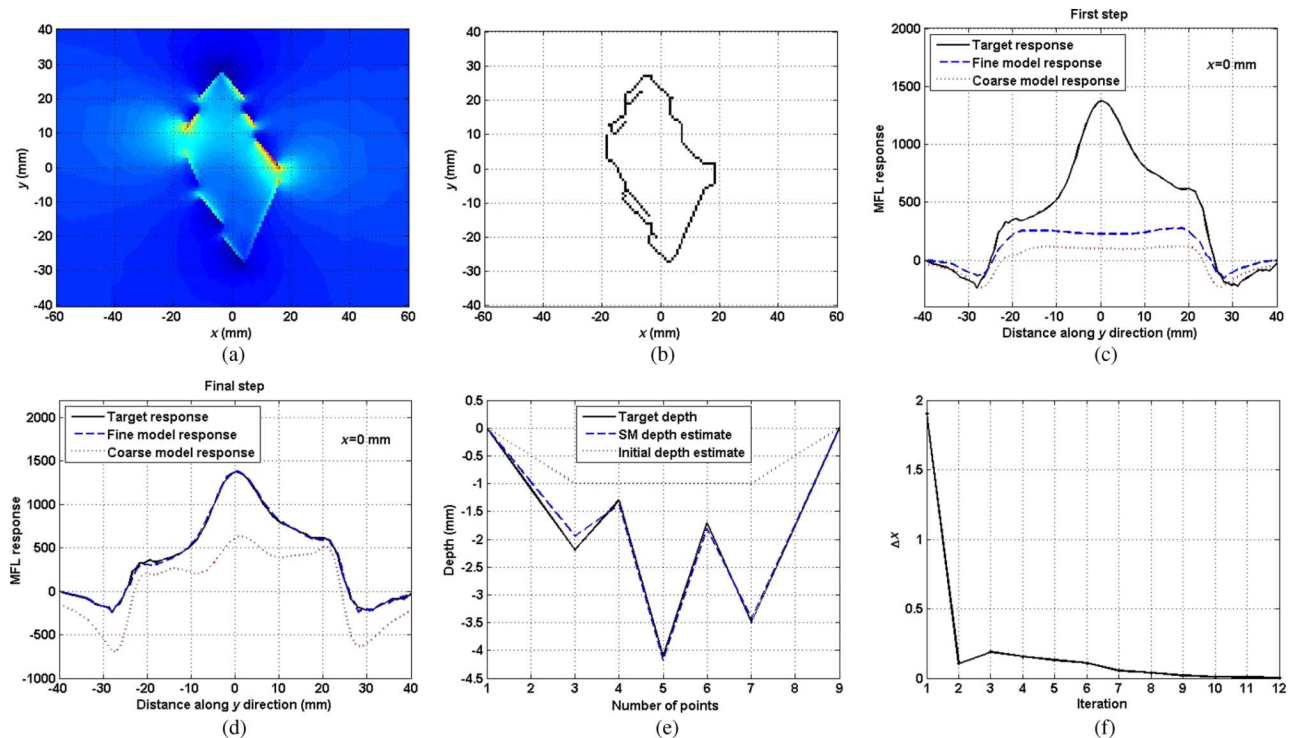


Fig. 8. (a) 2-D color map of the MFL signal for the defect of Fig. 5(c); (b) the defect opening (top view) detected by the Canny algorithm; (c), (d) comparison of the target MFL response with the MFL responses of the coarse and fine models obtained at initial and optimal points, respectively, at $x = 0$ mm and (e) their corresponding defect depth profile; (f) Δx in (11) versus iterations.

also compares the results of this method with direct optimization of the fine model using sequential quadratic programming (SQP). As the table shows, the direct optimization converges after 128, 113, and 142 fine model evaluations for defects in Figs. 5 (a), (b), and (c), respectively. It should be noted that a

single FEM simulation takes about 10 min of CPU time using an Intel Core 2 Duo processor at 2.4 GHz. This means that the direct optimization of the fine model requires at least 18.5 h of CPU time while SM optimization requires only about 1.5 h on average. Thus, the direct optimization of the fine model is far

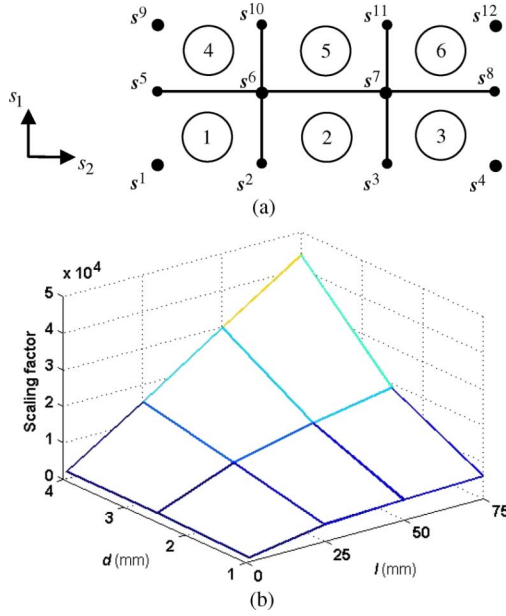


Fig. 9(a). Constructing the scaling surface from six sub-surfaces and twelve points (rectangular defects); (b) Scaling surface for rectangular defects.

TABLE I
CRACKS (POINTS) USED TO DEFINE SIX SUB-SURFACES IN FIG. 9

Region No.	Defect vertex No.	Parameter Region
1	1, 2, 5, 6	$s_1 \leq 2.5, s_2 \leq 25$
2	2, 3, 6, 7	$s_1 \leq 2.5, 25 \leq s_2 \leq 50$
3	3, 4, 7, 8	$s_1 \leq 2.5, s_2 \geq 50$
4	5, 6, 9, 10	$s_1 \geq 2.5, s_2 \leq 25$
5	6, 7, 10, 11	$s_1 \geq 2.5, 25 \leq s_2 \leq 50$
6	7, 8, 11, 12	$s_1 \geq 2.5, s_2 \geq 50$

more computationally expensive than SM optimization. Also, corresponding values of MRE are 56.2, 61.4, and 43.7, respectively. These large errors demonstrate that the direct optimization leads to the local minima in both cases, which are not the best solutions available. In contrast, SM optimization actually converges to the true solutions with much smaller MRE.

To further examine the performance of the proposed method, we apply it to the reconstruction of the shape of two real 3-D metal-loss defects whose MFL signals are obtained through measurement. The shapes of the defects opening (top view) are shown in Fig. 10. During the inspection process, the Hall sensor is placed at a liftoff distance $l_0 = 2.2$ mm above the surface of the metal. This nonzero liftoff value tends to affect the desired characteristics (i.e., smear out the sharp variation) in the MFL signal. This phenomenon decreases the accuracy of the defect opening extraction. In the MFL technique, mathematical modeling can be presented to show the effect of liftoff in the Fourier domain. Neglecting the displacement current, the components of the magnetic field above the metal surface satisfy the Laplace equation:

$$\nabla^2 H_i = 0 \quad i = x, y, z. \quad (16)$$

Using 2-D Fourier transforms in x and y , the solution for the magnetic field components at the liftoff l_0 above the metal

surface is found as [28]:

$$\tilde{H}_i(\alpha, \beta, l_0) = \tilde{H}_i(\alpha, \beta, 0) e^{-l_0 \sqrt{\alpha^2 + \beta^2}} \quad (17)$$

where α and β are the Fourier variables associated with the x and y directions and $\tilde{H}_i(\alpha, \beta, 0)$ and $\tilde{H}_i(\alpha, \beta, l_0)$ are the 2-D Fourier transforms of the magnetic field at the surface and at a distance l_0 from the surface, respectively.

Equation (17) shows that the nonzero value of the liftoff acts as a low-pass filter $G(\alpha, \beta, l_0) = e^{-l_0 \sqrt{\alpha^2 + \beta^2}}$. Therefore, the magnetic field distribution on the surface of the metal, $H_i(x, y, 0)$ can be restored by a deconvolution of the corresponding blurred sensor output signal, $H_i(x, y, l_0)$, which can be interpreted as a division operation in the frequency domain as follows:

$$\tilde{H}_i(\alpha, \beta, 0) = \frac{\tilde{H}_i(\alpha, \beta, l_0)}{G(\alpha, \beta, l_0)} \quad (18)$$

Figs. 11(a) and (b) and 12(a) and 12(b) show a 2-D color map of the measured and reconstructed (using (18)) surface signals for the two defects shown in Figs. 10(a) and (b), respectively. We then apply the Canny edge detection algorithms on these reconstructed signals to extract the defects opening shape as shown in Figs. 11(c) and 12(c). Because we may have some discontinuity in the Canny results where the edge of the defect is near to the perpendicular to the applied magnetic field, we then connect these disconnected parts together by lines. For the purpose of estimating the defects' depth profile, one row of the surface MFL signals that passes across the major portion of the defects ($H_y(x, 0, 0)$) are selected as input entries to SM optimization algorithm, Figs. 11(d) and 12(d). Figs. 11(d), 11(e), 12(d), and 12(e) show the target MFL response and the MFL responses of the coarse and fine models obtained at the initial and optimal points for the two defects of Fig. 10. The comparisons of the actual depth profile with the initial and optimal estimated depth profiles are shown in Figs. 11(f) and 12(f). As the figures show, the maximum depth of the defect has been detected accurately while the estimated depth profile cannot follow accurately sharp variations in the actual profile. Here, the detection area of the Hall sensor is 3 mm \times 4 mm. This extent of area of the sensor introduces a low-pass filtering effect on the MFL signal, which affects the resolution ability of the measurement setup and eliminates sharp variations of the MFL signal. This phenomenon leads to a smooth estimation of the defect opening shape and depth profile and reduces the ability to estimate sharp variations. The 3-D views of the reconstructed defects are shown in Fig. 13. Fig. 14 shows the convergence characteristic of SM algorithm for the two defects of Fig. 10. This figure shows that the SM algorithm converges to the optimal point in just 7 and 6 iterations for the defects of Figs. 10(a) and 10(b), respectively. The MRE values in both cases are given in Table III. As can be seen in this table, while the value of MRE for the depth profile is relatively high, the value of MRE for the maximum depth, which is of utmost interest in practical applications, is less than 6.5%.

VIII. CONCLUSION

This paper presents an inversion approach for estimating the shape of the opening and the depth profile of an arbitrary 3-D

TABLE II
ERRORS IN THE PREDICTION OF THE DEFECTS DEPTH PROFILES SHOWN IN FIGS. 6, 7, AND 8

Defect	MRE for SM optimization	Number of fine model evaluations (SM optimization)	CPU time (hours)	MRE for direct optimization	Number of fine model evaluations (direct optimization)	CPU time (hours)
Fig. 6(e)	5.97	9	1:30	56.2	128	21:20
Fig. 7(e)	9.11	8	1:20	61.4	113	18:50
Fig. 8(e)	5.63	12	2	43.7	142	23:40

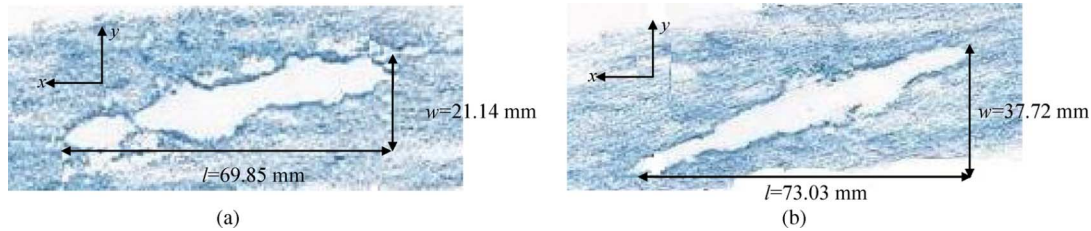


Fig. 10. 2-D view of the opening of two measured arbitrary defects.

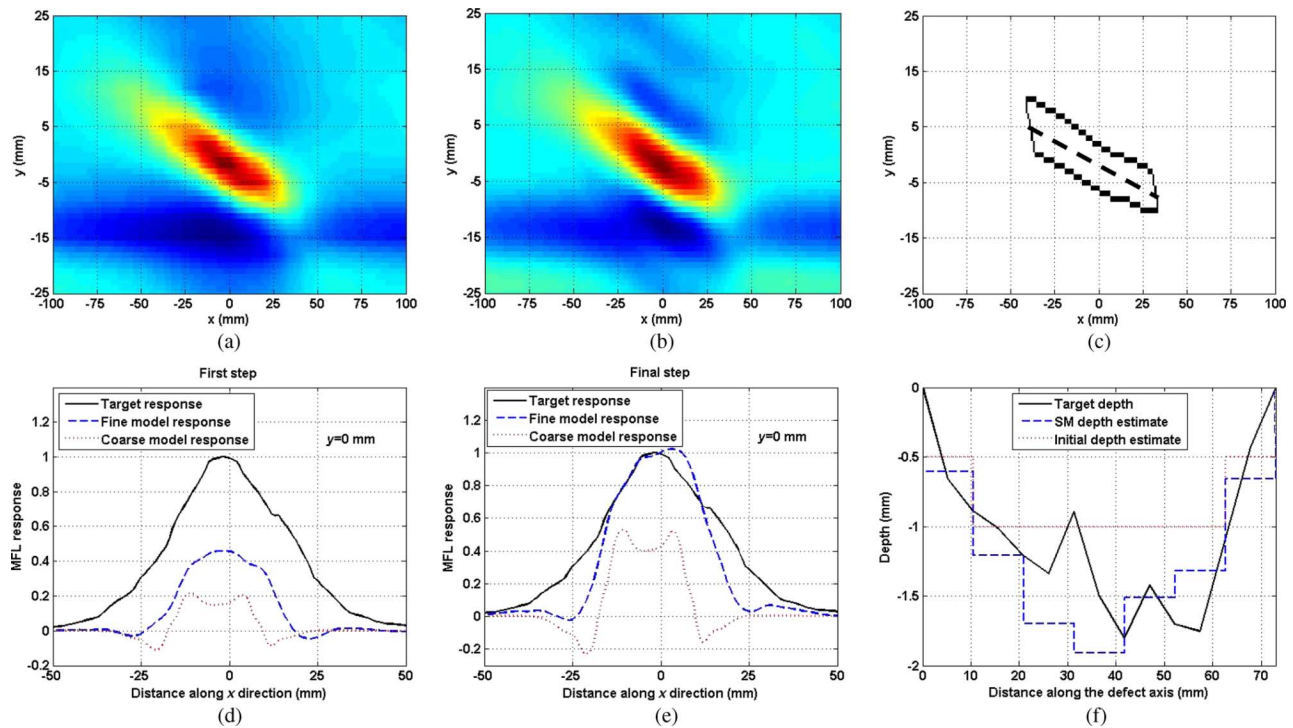


Fig. 11. (a) 2-D color map of the MFL signal for the defect of Fig. 10(a) when the sensor scans the metal surface at a liftoff distance $l_o = 2.2$ mm; (b) its respective restored surface counterpart; (c) the Canny edge detector result; (d), (e) comparison of the normalized target MFL response with the MFL responses obtained at the SM initial point and optimal point respectively, at $y = 0$ mm and (f) their corresponding defect depth profile along the defect axis [dashed line in (c)].

defect from MFL signals. The ultimate goal is to estimate accurately the maximum depth of the defect. In this method, first the Canny edge detection algorithm is applied to the 2-D color map of the MFL signal to detect the shape of the defect opening. This reduces the number of optimizable parameters and improves the defect characterization. The SM optimization algorithm is then used to estimate the defect depth profile. The proposed method was first tested and verified for three different defects with simulated MFL signals. The results demonstrated that the Canny edge detector can precisely detect the shape of the defect opening. Also, the SM inversion technique can estimate the defect depth profile accurately with just a few fine model evaluations. To examine the performance of the proposed method in practical examples, we applied it to the reconstruction of two real metal-loss defects whose MFL signals are measured. In this

case the nonzero liftoff distance of the Hall sensor from the surface of the metal acts as a low-pass filter which affects the accuracy of the defect geometry estimation. Therefore, we first restore the surface signal by a deconvolution process. Then we use the restored signal to estimate the shape of the opening and the depth profile. The results demonstrate that the area of the Hall sensor eliminates sharp variations of the signal. This affects the accuracy of the defect opening shape and depth profile estimation. However, the maximum depth of the defect has been detected accurately which is of utmost interest in practical applications.

ACKNOWLEDGMENT

This research was supported by a collaborative research development (CRD) grant of the Natural Sciences and En-

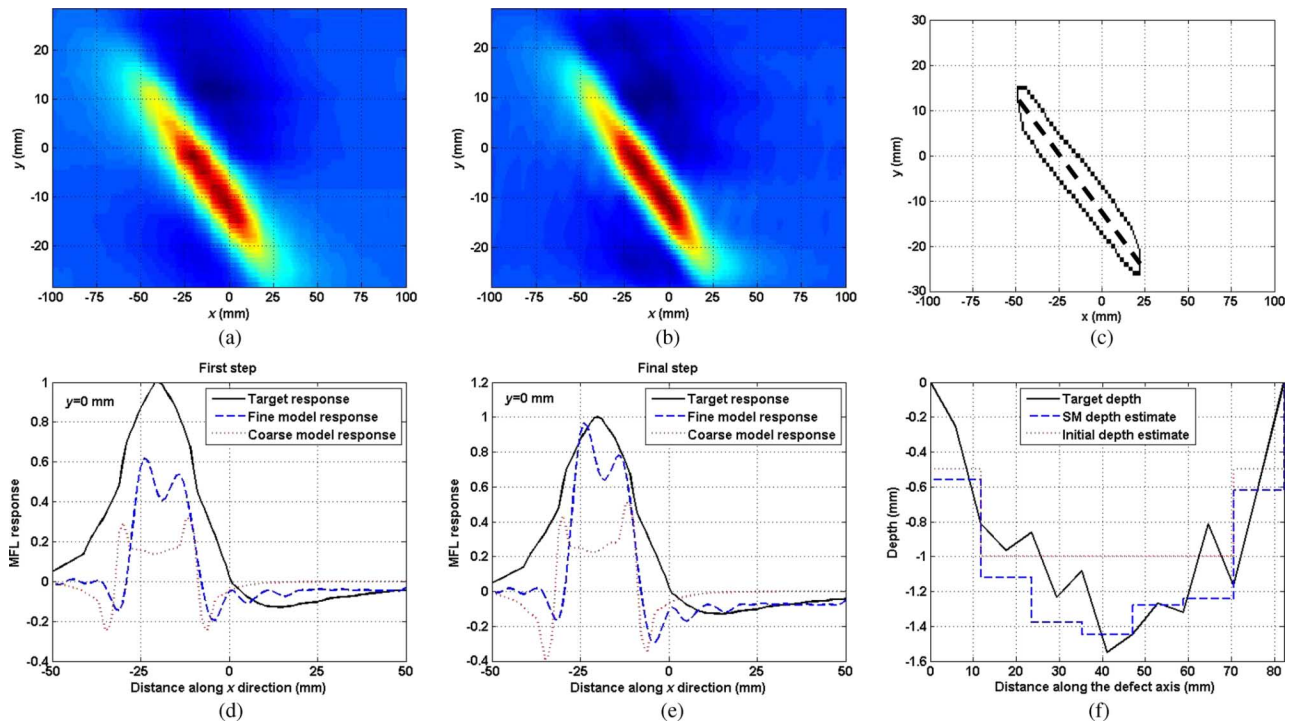


Fig. 12. (a) 2-D color map of the MFL signal for the defect of Fig. 10(b) when the sensor scans the metal surface at a liftoff distance $l_o = 2.2$ mm; (b) its respective restored surface counterpart; (c) the Canny edge detector result; (d), (e) comparison of the normalized target MFL response with the MFL responses obtained at the SM initial point and optimal point respectively, at $y = 0$ mm and (f) their corresponding defect depth profile along the defect axis [dashed line in (c)].

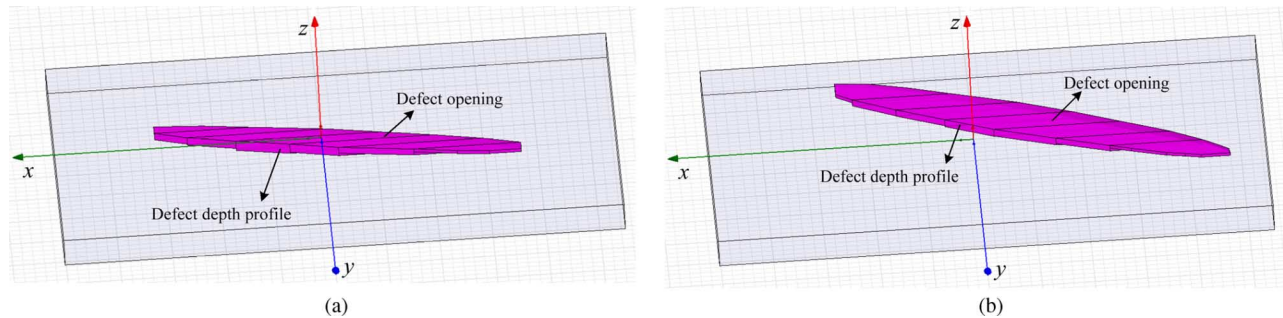


Fig. 13. (a), (b) 3-D view of the reconstructed counterparts of the defects of Figs. 10(a) and (b), respectively, in Maxwell v. 11.

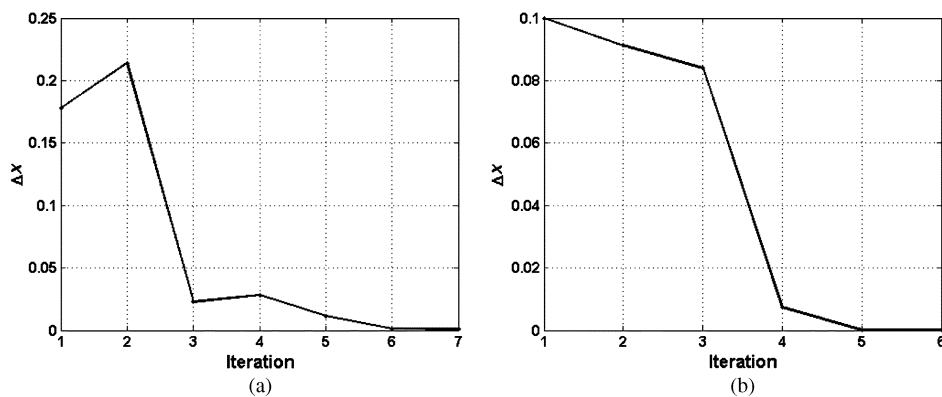


Fig. 14. (a), (b) Δx in (11) versus iterations for the defects of Figs. 10(a) and (b), respectively.

TABLE III
ERRORS IN THE PREDICTION OF THE LENGTH, WIDTH, AND DEPTH OF THE DEFECTS IN FIG. 10

Defect	\hat{l}	MRE (length)	\hat{w}	MRE (width)	MRE (depth profile)	MRE (maximum depth)
Fig. 10(a)	73	4.51	20	5.40	23.18	4.77
Fig. 10(b)	71	2.78	41	8.70	19.12	6.45

gineering Council of Canada (NSERC) and Intratech Inline Inspection Services Ltd., under Grant CRDPJ 349624-06. The authors are grateful to J. Hare of Intratech Inline Inspection Services Ltd. for many fruitful discussions and for providing much technical detail with regard to the measured data and the MFL measurement hardware.

REFERENCES

- [1] S. Hoole, "Artificial neural networks in the solution of inverse electromagnetic field problems," *IEEE Trans. Magn.*, vol. 29, no. 2, pp. 1931–1934, Mar. 1993.
- [2] R. Sikora, T. Chady, and J. Sikora, "Neural network approach to crack identification," *Int. J. Appl. Electromagn. Mech.*, vol. 9, no. 4, pp. 391–398, 1997.
- [3] P. Ramuhalli, L. Udpa, and S. Udpa, "Neural network algorithm for electromagnetic NDE signal inversion," in *Electromagnetic Nondestructive Evaluation (V)*. Amsterdam, The Netherlands: IOS, 2001, pp. 121–128.
- [4] R. Schifini and A. C. Bruno, "Experimental verification of a finite element model used in a magnetic flux leakage inverse problem," *J. Phys. D: Appl. Phys.*, vol. 38, no. 12, pp. 1875–1880, Jun. 2005.
- [5] Z. Chen, G. Preda, O. Mihalache, and K. Miya, "Reconstruction of crack shapes from the MFLT signals by using a rapid forward solver and an optimization approach," *IEEE Trans. Magn.*, vol. 38, no. 2, pp. 1025–1028, Mar. 2002.
- [6] M. Yan, S. Udpa, S. Mandayam, Y. Sun, P. Sacks, and W. Lord, "Solution of inverse problems in electromagnetic NDE using finite element methods," *IEEE Trans. Magn.*, vol. 34, no. 5, pp. 2924–2927, Sep. 1998.
- [7] C. Mandache and L. Clapham, "A model for magnetic flux leakage signal predictions," *J. Phys. D: Appl. Phys.*, vol. 36, no. 20, pp. 2427–2431, Oct. 2003.
- [8] D. Minkov, J. Lee, and T. Shoji, "Study of crack inversions utilizing dipole model of a crack and Hall element measurements," *J. Magn. Magn. Mater.*, vol. 217, no. 1, pp. 207–215, Jul. 2000.
- [9] D. Minkov and T. Shoji, "Method for sizing of 3-D surface breaking flaws by leakage flux," *NDT & E Int.*, vol. 31, no. 5, pp. 317–324, 1998.
- [10] C. Edwards and S. B. Palmer, "The magnetic leakage field of surface-breaking cracks," *J. Phys. D: Appl. Phys.*, vol. 19, no. 4, pp. 657–673, Apr. 1986.
- [11] A. Joshi, L. Udpa, S. Udpa, and A. Tamburrino, "Adaptive wavelets for characterizing magnetic flux leakage signals from pipeline inspection," *IEEE Trans. Magn.*, vol. 42, no. 10, pp. 3168–3170, Oct. 2006.
- [12] P. Ramuhalli, L. Udpa, and S. S. Udpa, "Electromagnetic NDE signal inversion by function-approximation neural networks," *IEEE Trans. Magn.*, vol. 38, no. 6, pp. 3633–3642, Nov. 2002.
- [13] P. Ramuhalli, L. Udpa, and S. S. Udpa, "Neural network-based inversion algorithms in magnetic flux leakage nondestructive evaluation," *J. Appl. Phys.*, vol. 93, no. 10, pp. 8274–8276, May 2003.
- [14] W. Bandler, R. M. Biernacki, S. H. Chen, P. A. Grobelny, and R. H. Hemmers, "Space mapping technique for electromagnetic optimization," *IEEE Trans. Microw. Theory Tech.*, vol. 2, no. 12, pp. 2536–2544, Dec. 1994.
- [15] J. W. Bandler, Q. S. Cheng, D. H. Gebre-Mariam, K. Madsen, F. Pedersen, and J. Søndergaard, "EM-based surrogate modeling and design exploiting implicit, frequency and output space mappings," in *IEEE MTT-S Int. Microw. Symp. Dig.*, Philadelphia, PA, Jun. 2003, pp. 1003–1006.
- [16] J. W. Bandler, Q. S. Cheng, S. A. Dakroury, A. S. Mohamed, M. H. Bakr, K. Madsen, and J. Søndergaard, "Space mapping: The state of the art," *IEEE Trans. Microw. Theory Tech.*, vol. 52, no. 1, pp. 337–361, Jan. 2004.
- [17] D. Echeverria and P. W. Hemker, "Space mapping and defect correction," *CMAM The International Mathematical Journal Computational Methods in Applied Mathematics*, vol. 5, no. 2, pp. 107–136, 2005.
- [18] J. W. Bandler, S. Koziel, and K. Madsen, "Space mapping for engineering optimization," *SIAG/Optimization Views-and-News Special Issue on Surrogate/Derivative-Free Optimization*, vol. 17, no. 1, pp. 19–26, 2006.
- [19] S. Koziel, J. W. Bandler, and K. Madsen, "A space-mapping framework for engineering optimization: Theory and implementation," *IEEE Trans. Microw. Theory Tech.*, vol. 54, no. 10, pp. 3721–3730, Oct. 2006.
- [20] R. K. Amineh, S. Koziel, N. K. Nikolova, J. W. Bandler, and J. P. Reilly, "A space mapping methodology for defect characterization from magnetic flux leakage measurements," *IEEE Trans. Magn.*, vol. 44, no. 8, pp. 2058–2065, Aug. 2008.
- [21] Y. Li, L. Udpa, and S. S. Udpa, "Three-dimensional defect reconstruction from eddy-current NDE signals using a genetic local search algorithm," *IEEE Trans. Magn.*, vol. 40, no. 2, pp. 410–417, Mar. 2004.
- [22] J. F. Canny, "A computational approach to edge detection," *IEEE Trans. Pattern Anal. Mach. Intell.*, vol. 8, no. 6, pp. 679–698, Nov. 1986.
- [23] G. S. Park and E. S. Park, "Improvement of the sensor system in magnetic flux leakage-type nondestructive testing (NDT)," *IEEE Trans. Magn.*, vol. 38, no. 2, pp. 1277–1280, Mar. 2002.
- [24] Maxwell Version 11.1.1 Ansoft Corporation [Online]. Available: <http://www.ansoft.com>, 2006.
- [25] R. K. Amineh, N. K. Nikolova, J. P. Reilly, and J. R. Hare, "Characterization of surface breaking cracks using one tangential component of magnetic leakage field," *IEEE Trans. Magn.*, vol. 44, no. 4, pp. 516–524, Apr. 2008.
- [26] Matlab ver. 7.1, The MathWorks, Inc., Natick, MA, 2005.
- [27] S. Koziel and J. W. Bandler, "SMF: A user-friendly software engine for space-mapping-based engineering design optimization," in *Int. Symp. Signals, Systems and Electronics, URSI ISSSE 2007*, pp. 157–160.
- [28] R. K. Amineh, M. Ravan, S. H. H. Sadeghi, and R. Moini, "Removal of probe liftoff effects on crack detection and sizing in metals by the AC field measurement technique," *IEEE Trans. Magn.*, vol. 44, no. 8, pp. 2066–2073, Aug. 2008.